arXiv:1806.05669v1 [nucl-th] 14 Jun 2018

Probing the in-Medium QCD Force by Open Heavy-Flavor Observables

Shuai Y.F. Liu,[1] Min He,[2] and Ralf Rapp[1]

[1] *Cyclotron Institute and Department of Physics and Astronomy, Texas A&M University, College Station, TX 77843-3366, USA*

[2] *Department of Applied Physics, Nanjing University of Science and Technology, Nanjing 210094, China*

(Dated: December 2, 2021)

The determination of the color force in a quark-gluon plasma (QGP) is a key objective in the investigation of strong-interaction matter. Open and hidden heavy-flavor observables in heavy-ion collisions (HICs) are believed to provide insights into this problem by comparing calculations of heavy-quark (HQ) and quarkonium transport with pertinent experimental data. In this work, we utilize the T-matrix formalism to compute charm-quark transport coefficients for various input potentials previously extracted from simultaneous fits to lattice-QCD data for HQ free energies, quarkonium correlators and the QGP equation of state. We investigate the impact of off-shell effects (spectral functions) in the QGP medium on the HQ transport, and compare to earlier results using the free or internal HQ energies as potential proxies. We then employ the transport coefficients in relativistic Langevin simulations for HICs to test the sensitivity of heavy-flavor observables to the HQ interactions in the QGP. We find that a strongly-coupled T-matrix solution generates a HQ elliptic flow comparable to the results from the internal energy at low momentum, driven by a long-range remnant of the confining force, while falling off stronger with increasing 3-momentum. The weakly coupled T-matrix solution, whose underlying potential is close to the free energy, leads to an elliptic flow well below the experimentally observed range.

PACS numbers: 25.75.Dw, 12.38.Mh, 25.75.Nq
Keywords: Heavy-Flavor Transport, Quark Gluon Plasma, Ultrarelativistic Heavy-Ion Collisions

I. INTRODUCTION

The investigation of the in-medium color force between partons is pivotal for understanding the microscopic mechanisms that lead to the remarkable features of the quark-gluon plasma (QGP) as observed in ultrarelativistic heavy-ion collisions (URHICs). Lattice-QCD (lQCD) computations of the free energy of a heavy quark-antiquark ($Q\bar{Q}$) pair immersed into the QGP [1, 2] indicate that nonperturbative effects, specifically remnants of the linear part of the potential, survive up to temperatures of at least twice the pseudo-critical one, $T_{\rm pc} \simeq 160\,$MeV [3, 4]. Potential models [5–9] have been employed to implement these effects and test them against lQCD data for euclidean quarkonium correlators [10–13], but no definite answer on the modifications of the QCD force in medium could be achieved. To broaden these investigations we have been developing a thermodynamic T-matrix approach [9, 14–16] where consequences of the in-medium potential are assessed not only for quarkonia, but also for individual heavy quarks (such as their transport properties) and the surrounding medium that they interact with. The T-matrix framework has been solved selfconsistently for one- and two-parton correlations in a full off-shell scheme beyond the quasiparticle approximation [15, 16], allowing for the dynamical formation of (broad) bound states, and connecting bulk and microscopic properties of the QGP and its excitations (spectral functions). Despite constraints from three sets of lQCD data (equation of state (EoS), heavy-quark (HQ) free energy, and quarkonium correlators), the underlying in-medium potential could still not be determined unambiguously [16]. However, different potentials predict markedly different spectral and transport properties of the QGP. The objective of the present paper is to further explore this sensitivity by computing the thermal relaxation rates for charm quarks for different potential solutions (including previously used internal- and free-energy proxies) and quantifying their effect on the charm-quark spectra in URHICs using relativistic Langevin simulations. We specifically scrutinize off-shell effects in the calculation of the transport coefficients, which can play a significant role given the large spectral widths of partons found in the "strongly-coupled solution" of the T-matrix approach, together with broad D-meson resonance states in the charm-light-quark scattering amplitude near or even below the nominal two-parton threshold.

This paper is organized as follows. In Sec. II we recollect the main features and differences of weakly- and strongly-coupled solutions that we previously found within the T-matrix approach. In Sec. III we introduce the off-shell formalism to calculate HQ transport coefficients, and discuss an improved partial-wave expansion in the T-matrix over previous calculations of the HQ relaxation rate. In Sec. IV we analyze the results of the HQ transport coefficients from the different types of potentials. In Sec. V, we briefly recall the transport implementation into URHICs using relativistic Langevin simulations, calculate the charm-quark and D-meson nuclear modification factors (R_{AA}) and elliptic flow (v_2), and discuss the results in light of discriminating different potential strengths via experimental observables. In Sec. VI we summarize and conclude. In appendix A, we collect the expressions used for the transformation of the off-shell T-matrix into the center-of-mass (CM) frame as used in

this work.

II. IN-MEDIUM POTENTIALS BASED ON LATTICE QCD

In Ref. [16] we deployed the T-matrix approach, together with the Luttinger-Ward Baym formalism, in a comprehensive fit to lQCD data for the HQ free energy, quarkonium correlators and the QGP EoS. It turned out that the input potential required to simultaneously describe the lattice data is not unique. We bracketed the range of viable potentials by approximately limiting scenarios referred to as a strong-coupling scenario (SCS) and a weak-coupling scenario (WCS). The main features of the SCS are large thermal parton widths leading to a dissolution of their quasiparticle peaks at low momentum near $T_{\rm pc}$ while broad mesonic and diquark bound states emerge whose contribution dominates the pressure when approaching $T_{\rm pc}$ from above. On the other hand, in the WCS thermal partons remain well defined quasiparticles (with masses similar to the SCS), while rather narrow, loosely-bound two-body states form near $T_{\rm pc}$ whose contribution to the EoS remains, however, subleading. The underlying static potentials, V_s for the SCS and V_w for the WCS, are displayed in Fig. 1, along with the lQCD results for the free (F) and internal energy (U) that they reproduce through the T-matrix formalism. Both V_s and V_w lie in between U and F, and they tend to be closer to U as temperature increases while their gap diminishes. However, at low temperatures V_w essentially coincides with F while V_s reaches much above it at intermediate and especially large distances. This difference is the key factor in the resulting QGP spectral properties near $T_{\rm pc}$ as discussed above; the large-distance strength of V_s implies that the QGP is strongly coupled only at large distances, *i.e.*, for soft momenta.

Taking the derivative of the potentials, $-dV(r)/dr$, yields the pertinent forces, cf. Fig. 2. The forces for V_s and U at large distances are much higher than those for V_w and F. Around $r \simeq 0.5\,$fm and T=0.194 GeV, the force from U amounts to ca. 2.5 GeV/fm which even exceeds the vacuum force by about a factor of $\sim$2. This enhancement originates from the "entropy term", $-TdF/dT$, as a fast change in degrees of freedom near $T_{\rm pc}$ leads to a large temperature derivative. It has been suggested that this is caused by releasing thermal magnetic monopoles [17]. The force from V_s at this distance (at T=0.194 GeV) is also larger than in vacuum, by about 20%; *i.e.*, the major contribution to this force is still considered to be the remnant of the confining vacuum configuration rather than thermal monopoles.

The long-range force is closely related with low-momentum transport properties of the medium; in particular, a long-range force allows a parton to interact with an increased number of thermal partons in the heat bath, proportional to the volume of the spherical shell which grows as r^2. Therefore, by multiplying

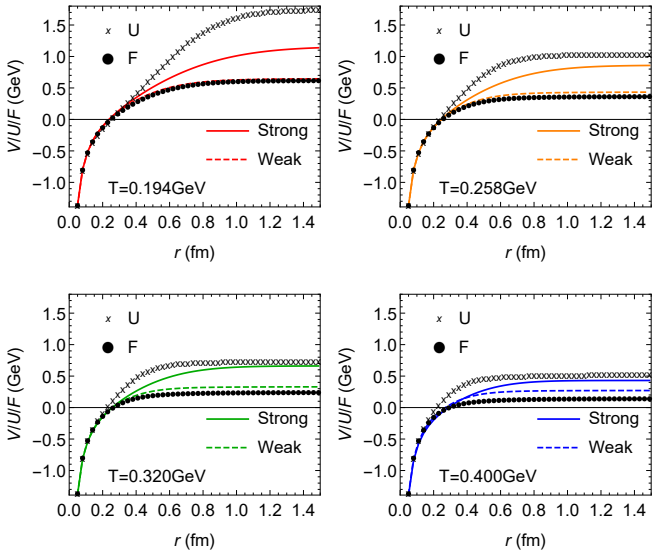


FIG. 1. The potentials of the SCS (solid lines) and WCS (dashed lines) are compared to the internal energy U (crosses) and free energy F (dots) as a function of distance between a Q and $\bar{Q}$, for four temperatures.

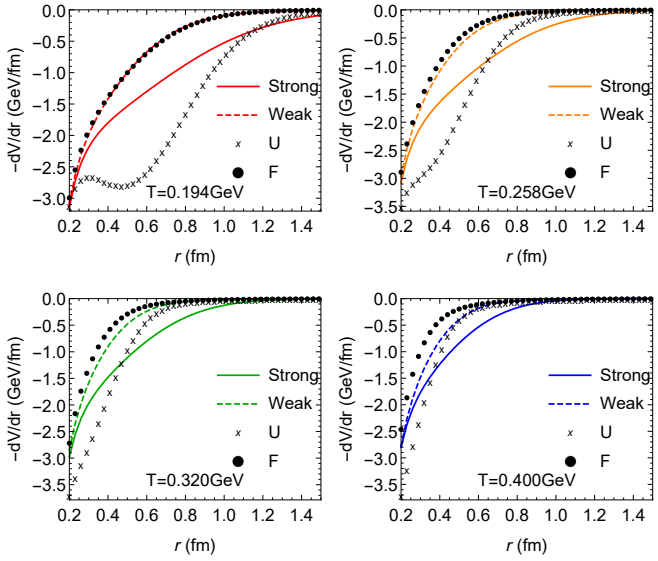


FIG. 2. Force for V_s (solid line), V_w (dashed line), U (crosses) and F (dots) at different temperatures.

the force with $\frac{3}{4}r^2$, one forms a dimensionless quantity, $\frac{3}{4}r^2 dV/dr$, that can be regarded as an "effective interaction strength" in the medium and is plotted for the 4 "potentials" in Fig. 3. The factor of 3/4 renders the $r \to 0$ limit equal to the strong coupling constant, which is α_s=0.27 for all of our 4 "potentials". Starting from short range, U has the largest interactions, up to $r \simeq 1(0.4)\,$fm at the smallest (largest) temperature, due to the "entropy-related" potential, $-TdF/dT$; as we will see below, this can affect transport properties even at rather high momentum. Coming from the large distance

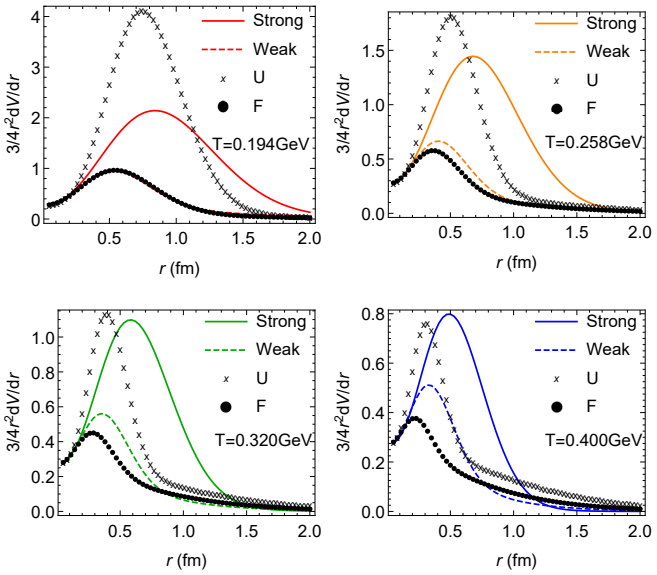


FIG. 3. The dimensionless quantity $\frac{3}{4}r^2dV/dr$ (scaled to recover the strong coupling constant, α_s, at short distance) is plotted for V_s (solid line), V_w (dashed line), U (crosses) and F (dots).

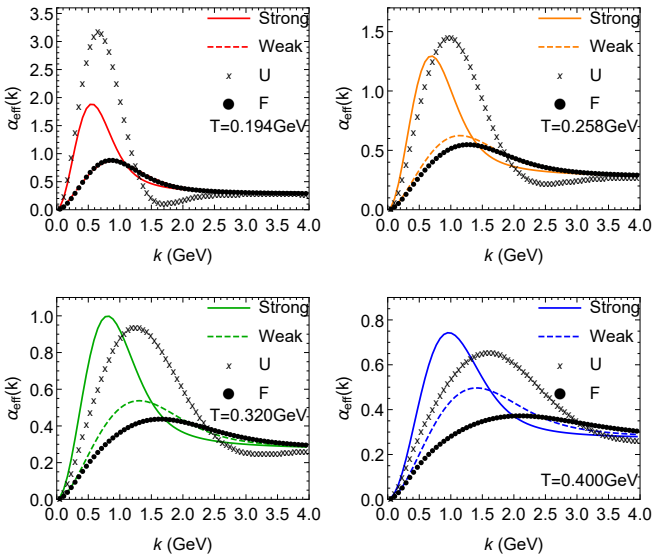


FIG. 4. The dimensionless quantity $\alpha_{\rm eff}(k) \equiv \frac{3}{16\pi}k^2V(k)$ (scaled to recover the strong coupling constant, α_s, at large momentum) is plotted for V_s (solid line), V_w (dashed line), U (crosses) and F (dots).

side, V_s gives the strongest "effective" coupling, and its maximum coupling peak at each temperature is located at the largest distance among all potentials, ranging from $r_{\rm max}$=0.85 fm at T=0.194 GeV down to $r_{\rm max}$=0.5 fm at T=0.400 GeV. The large-distance enhancement of the coupling can be related to an infrared enhancement in momentum space, as illustrated by the dimensionless-scaled momentum space potentials displayed in Fig. 4: here, the maximum interaction strength for V_s occurs at the lowest momentum (relative momentum exchange between Q and $\bar{Q}$) among the 4 potentials, approximately given by $p_{\rm max} = 2/r_{\rm max}$.

III. OFF-SHELL TRANSPORT COEFFICIENTS

As mentioned above, the strong color force, in particular in the SCS, leads to large widths in the spectral functions of thermal partons, dissolving their quasiparticle peaks at low momenta and temperatures [16]. It is therefore in order to incorporate the off-shell effects in the Boltzmann/Langevin description of the HQ transport. Toward this goal, we start from the Kadanoff-Baym equations and use a minimal set of approximations to reduce them to a Boltzmann equation, where quantum effects are encoded in the transition rates. Subsequently, this Boltzmann equation is expanded into a Fokker-Planck equation, which can be implemented via a Langevin process where quantum effects are encoded in the transport coefficients.

We closely follow the formalism for non-equilibrium quantum field theory described in Ref. [18]. We first illustrate a formal derivation of the relations for the non-relativistic case, but our final expressions for the transport coefficients account for relativistic effects as discussed in Ref. [16]. In relative energy-momentum space, with a macroscopic time denoted as t,[1] the equation for the non-equilibrium HQ Green function can be expressed as[2]

$$\frac{\partial}{\partial t}[\int d\omega G_Q^<(\omega,\mathbf{p},t)] = \int d\omega\{i\Sigma_Q^<(\omega,\mathbf{p},t)G_Q^>(\omega,\mathbf{p},t) - i\Sigma_Q^>(\omega,\mathbf{p},t))G_Q^<(\omega,\mathbf{p},t)\} \ . \quad (1)$$

The $G_Q^{<,>}(\omega,\mathbf{p},t)$ are the Fourier transforms of the Green functions,

$$G_Q^<(t_1,x_1,t_2,x_2) = i\langle\psi_Q^\dagger(t_2,x_2)\psi_Q(t_1,x_1)\rangle \quad (2)$$

$$G_Q^>(t_1,x_1,t_2,x_2) = -i\langle\psi_Q(t_1,x_1)\psi_Q^\dagger(t_2,x_2)\rangle \ , \quad (3)$$

with respect to δt and δx for fixed t and x where $\delta t = t_1 - t_2$, $\delta x = x_1 - x_2$, $t = (t_1+t_2)/2$, $x = (x_1+x_2)/2$ [18]. In a uniform medium the $G_Q^{<,>}$ do not depend on x. $\Sigma_Q^{<,>}$ is the selfenergy in the real-time formalism, in which it can be calculated diagrammatically from the underlying scattering processes between the heavy quark and the partons of the medium. The Fourier transform of $\Sigma_Q^{<,>}$ uses the same convention as that for $G_Q^{<,>}$. The T-matrix approach has been used to derive the expressions

[1] We use the same approximation, $T \pm t/2 \approx T$, as in Ref. [18], but use t to denote $T = (t_1+t_2)/2$.

[2] We enforce translational invariance so that all terms with a coordinate gradient vanish, and the Boltzmann equation used to evaluate the transport coefficients can be obtained as in Ref. [19].

for these selfenergies in Appendix F of Ref. [18]. One has

$$\Sigma_Q^>(\omega,\mathbf{p},t) = \mp\sum\int \frac{d\omega' d^4\mathbf{p}'}{(2\pi)^4}\frac{d\nu d^3\mathbf{q}}{(2\pi)^4}\frac{d\nu' d^4\mathbf{q}'}{(2\pi)^4}(2\pi)^4\delta^{(4)} \times |T(E,\mathbf{P},\mathbf{p},\mathbf{p}')|^2 G_Q^>(\omega',p')G_i^<(\nu,q)G_i^>(\nu',q') \ , \quad (4)$$

and

$$\Sigma_Q^<(\omega,\mathbf{p},t) = \mp\sum\int \frac{d\omega' d^4\mathbf{p}'}{(2\pi)^4}\frac{d\nu d^3\mathbf{q}}{(2\pi)^4}\frac{d\nu' d^4\mathbf{q}'}{(2\pi)^4}(2\pi)^4\delta^{(4)} \times |T(E,\mathbf{P},\mathbf{p},\mathbf{p}')|^2 G_Q^<(\omega',p')G_i^>(\nu,q)G_i^<(\nu',q') \ . \quad (5)$$

Here, $\delta^{(4)}$ is a short-hand notation for energy-momentum conservation, and $\sum$ represents the summation over the internal degrees of freedom $i = q, \bar{q}, g$ and their color, spin and flavor, divided by one HQ degeneracy, d_Q=6; $\mathbf{P}$ and E are the total momentum and energy, and $T(E,\mathbf{P},\mathbf{p},\mathbf{p}')$ is the retarded T-matrix. The $G_i^{<,>}$ are the Green functions for the light partons in medium. The classical Boltzmann equation is recovered from Eq. (1) using the on-shell approximations: $G^< = \mp i(2\pi)\delta(\omega-\varepsilon(\mathbf{p}))f(\mathbf{p},t))$ and $G^> = -i(2\pi)\delta(\omega-\varepsilon(\mathbf{p}))(1\pm f(\mathbf{p},t))$. These approximations are derived in Ref. [18];[3] they neglect off-shell quantum effects, but not all are necessary to describe HQ diffusion in a local-equilibrium QGP. We have found that "minimal" approximations required for obtaining a HQ Boltzmann equation amount to

$$\begin{aligned} G_Q^<(\mathbf{p},\omega,t) &= i(2\pi)\delta(\omega-\varepsilon_Q(\mathbf{p}))f_Q(\mathbf{p},t) \ , \\ G_Q^>(\omega,p) &= -i(2\pi)\rho_Q(\omega,p)(1-n_Q(\omega)) \ , \\ G_i^<(\omega,p) &= \mp i(2\pi)\rho_i(\omega,p)n_i(\omega) \ , \\ G_i^>(\omega,p) &= -i(2\pi)\rho_i(\omega,p)(1\pm n_i(\omega)) \ , \end{aligned} \quad (6)$$

where the quasiparticle approximation is only applied to $G_Q^<(\omega,\mathbf{p},t)$, *i.e.*, the incoming heavy quark, while all other $G^{<,>}$ are taken to be off-shell equilibrium Green functions, with $\rho_{i,Q}$ and $n_{i,Q}$ denoting the corresponding spectral and distribution functions, respectively, for light (i) and heavy (Q) partons in equilibrium. Substituting these expressions into Eqs. (1), (4), and (5), yields the Boltzmann equation

$$\frac{\partial}{\partial t}f(\mathbf{p},t) = \int\frac{d^3\mathbf{k}}{(2\pi)^3}[w(\mathbf{p}+\mathbf{k},\mathbf{k})f(\mathbf{p}+\mathbf{k},t) - w(\mathbf{p},\mathbf{k})f(\mathbf{p},t)] \ , \quad (7)$$

where the transition rate is[4]

$$w(\mathbf{p},\mathbf{k}) = \int\frac{d\nu d^3\mathbf{q}}{(2\pi)^3}\frac{d\nu' d^3\mathbf{q}'}{(2\pi)^3}d\omega'(2\pi)^4\delta^{(4)}\rho_i(\nu,q) \times \rho_i(\nu',q')\rho_Q(\omega',|\mathbf{k}+\mathbf{p}|)|T(E,\mathbf{P},\mathbf{p},\mathbf{k}+\mathbf{p})|^2 \times n_i(\nu)\left[1\mp n_i(\nu')\right]\left[1-n_Q(\omega')\right] \ , \quad (8)$$

and $\mathbf{k} = \mathbf{p}' - \mathbf{p}$ is the 3-momentum exchange. Note that we have approximated the distribution function of the outgoing heavy quark in the blocking factor $(1 - n_Q)$ to be a thermal one (the blocking factor is close to one in any case), and therefore the rate $w(\mathbf{p},\mathbf{k})$ does not depend on the dynamical non-equilibrium HQ distribution function, $f(\mathbf{p},t)$. So far, our discussion does not include relativistic effects; several modifications are necessary to do that, as detailed in the following for the calculation of the HQ transport coefficients.

Expanding the full Boltzmann equation in the momentum transfer, $\mathbf{k}$, results in a Fokker-Planck equation, which can be converted to a Langevin approach for heavy quarks. The Fokker-Planck equation is given by

$$\frac{\partial}{\partial t}f(p,t) = \frac{\partial}{\partial p_i}\{A_i(p)f(p,t) + \frac{\partial}{\partial p_j}[B_{ij}(p)f(p,t)]\} \quad (9)$$

where the HQ transport coefficients are defined as weighted averages over the transition rate,

$$\begin{aligned} A_i(p) &= \int\frac{d^3\mathbf{k}}{(2\pi)^3}w(\mathbf{p},\mathbf{k})k_i \\ B_{ij}(p) &= \int\frac{1}{2}\frac{d^3\mathbf{k}}{(2\pi)^3}w(\mathbf{p},\mathbf{k})k_ik_j \ . \end{aligned} \quad (10)$$

In local equilibrium, the drag (A) and transverse/longitudinal diffusion coefficients (B_0/B_1) are defined through

$$\begin{aligned} A_i(p) &= A(p)p_i \\ B_{ij}(p) &= B_0(p)P_{ij}^\perp + B_1(p)P_{ij}^\parallel \ , \end{aligned} \quad (11)$$

with the projectors $P_{ij}^\perp = \delta_{ij} - p_ip_j/\mathbf{p}^2$ and $P_{ij}^\parallel = p_ip_j/\mathbf{p}^2$. The scalar transport coefficients, $A(p)$, $B_0(p)$ and $B_1(p)$, can thus be expressed via averages

$$\langle X(\mathbf{p}')\rangle \equiv \int\frac{d^3\mathbf{k}}{(2\pi)^3}w(\mathbf{p},\mathbf{k})X(\mathbf{p}') \quad (12)$$

as

$$\begin{aligned} A(p) &= \langle 1 - \frac{\mathbf{p}\cdot\mathbf{p}'}{\mathbf{p}^2}\rangle \\ B_0(p) &= \frac{1}{2}\langle p'^2 - \frac{(\mathbf{p}\cdot\mathbf{p}')^2}{\mathbf{p}^2}\rangle \\ B_1(p) &= \frac{1}{2}\langle\frac{(\mathbf{p}\cdot\mathbf{p}')^2}{\mathbf{p}^2} - 2\mathbf{p}\cdot\mathbf{p}' + \mathbf{p}^2\rangle \ . \end{aligned} \quad (13)$$

Using the expression for $w(\mathbf{p},\mathbf{k})$ in Eq. (8) with the replacement $\mathbf{k}-\mathbf{p}\to\mathbf{p}'$, and switching the integration variable to $\mathbf{p}'$, we express $\langle X(\mathbf{p}')\rangle$ in T-matrix form as

$$\langle X(\mathbf{p}')\rangle = \sum_i\frac{1}{2\varepsilon_Q(p)}\int\frac{d\omega' d\mathbf{p}'}{(2\pi)^3 2\varepsilon_Q(p')}\frac{d\nu d^3\mathbf{q}}{(2\pi)^3 2\varepsilon_i(q)}\frac{d\nu' d^3\mathbf{q}'}{(2\pi)^3 2\varepsilon_i(q')} \times\delta^{(4)}\frac{(2\pi)^4}{d_Q}\sum_{a,l,s}|M|^2\rho_Q(\omega',p')\rho_i(\nu,q)\rho_i(\nu',q') \times[1-n_Q(\omega')]n_i(\nu)[1\pm n_i(\nu')]X(\mathbf{p}') \ . \quad (14)$$

[3] Our convention for "$\mp$" (upper/lower sign denotes boson/fermion) is opposite of that in Ref. [18].

[4] Note that $i\Sigma^>(p,\varepsilon(p),t)f(\mathbf{p},t) = \int\frac{d^3\mathbf{k}}{(2\pi)^3}[w(\mathbf{p},\mathbf{k})f(\mathbf{p},t)]$. Also, when converting the gain term, $\Sigma_Q^<G_Q^>$, to Boltzmann form, it is necessary to use $T(E,\mathbf{P},\mathbf{p},\mathbf{p}') = T(E,\mathbf{P},\mathbf{p}',\mathbf{p})$.

The summation $\sum_i$ is over all light flavors, $i = u, \bar{u}, d, \bar{d}, s, \bar{s}, g$, where the light and strange quarks are assumed to have the same mass (which is a good approximation in our context [9]). We include the relativistic phase space factor with the single-particle on-shell energy, denoted by $\varepsilon_{Q,i}(p)$. The heavy-light scattering matrix elements, $|M_{Qi}|^2$, in Eq. (14) are related to the T-matrix in the CM frame as

$$\sum_{a,l,s} |M^2| = 16\varepsilon_Q(p_{\rm cm})\varepsilon_i(p_{\rm cm})\varepsilon_Q(p'_{\rm cm})\varepsilon_i(p'_{\rm cm})]d_s^{Qi} \times \sum_a d_a^{Qi} \left| 4\pi \sum_l (2l+1) T_{Q,i}^{a,l}(E_{\rm cm}, p_{\rm cm}, p'_{\rm cm}) P_l\left(\cos\theta_{\rm cm}\right) \right|^2 , \tag{15}$$

where $T_{Qi}^{a,l}(E_{\rm cm}, p_{\rm cm}, p'_{\rm cm})$ is calculated in the CM frame in all possible two-body color channels, a, and partial-wave channels, l. The CM energy, $E_{\rm cm}$, incoming CM momentum $p_{\rm cm}$, outgoing CM momentum $p'_{\rm cm}$, and scattering angle $\cos\theta_{\rm cm}$ are expressed as functions of E, $\mathbf{p}$, $\mathbf{q}$, $\mathbf{p}'$, $\mathbf{q}'$, as discussed in App. A. The two-body color/spin degeneracy factor is denoted by $d_{a,s}^{Qi}$, and the $P_l\left(\cos\theta_{\rm cm}\right)$ are Legendre polynomials. The partial-wave summation is different from that employed in Eq. (8) of Ref. [20] (and in Ref. [9]), in that our expression (15) includes the interference effects between different partial waves and an additional factor of π. We also carry the partial-wave expansion to higher angular momenta of up to l=8 (compared to l=1 in Refs. [9, 20]), which turns out to be essential for the convergence of the high-momentum region of the transport coefficients. More explicitly, one can show that $|\sum_l (2l+1)c_l P_l(x)|^2 = \sum_l (2l+1) b_l P_l(x)$, where each b_l is a function of the $\{c_l\}$. The final results for the friction coefficient using, *e.g.*, the U potential turn out to be within ∼20% of the results of Ref. [9] based on the same lQCD free-energy data. This is a consequence of benchmarking the partial-wave expansion in both versions against the full perturbative-QCD (pQCD) results.

IV. CHARM QUARK TRANSPORT COEFFICIENTS

In this section, we discuss the resulting charm-quark transport coefficients, focusing on the drag coefficient $A(p)$ which characterizes the thermal relaxation rate for the different input potentials. We emphasize that the "true" potentials V_s and V_w are part of a comprehensive many-body set-up which encompasses the lQCD EoS and thus fully specifies the properties of thermal medium, *i.e.*, the spectral functions (masses and widths) of the thermal partons that the heavy quark scatters off. This is not the case for the previously used potential "proxies" F and U, which have been applied within quasiparticle approximations for the QGP medium. Therefore, in Sec. IV A, we first conduct baseline calculations for all four potentials, $\{U, F, V_s, V_w\}$, with thermal quasiparticle partons. In Sec. IV B, we employ the off-shell formalism outlined above to compute the transport coefficients for the potentials $\{V_s, V_w\}$ in their accompanying bulk medium. In Sec. IV C we scrutinize various nonperturbative effects (resummed vs. Born amplitudes, Coulomb vs. full calculations with string term, and on- vs. off-shell) to exhibit their quantitative role in the HQ transport.

A. Drag coefficients for different color forces in quasiparticle medium

We first restrict ourselves to the quasiparticle approximation for the QGP medium, *i.e.*, the thermal-parton spectral functions in the expressions given in Sec. III are taken to be δ-functions at their quasiparticle masses. The latter are chosen to be the same for all four potentials as shown in Fig. 5 left, obtained from a quasiparticle fit to the lQCD EoS using the Fock mass ansatz [16] with V_s. The charm-quark masses, plotted in Fig. 5 right, are taken to be $1.264 + \Sigma(\infty;T)/2$ where $\Sigma(\infty;T)$ denotes the infinite-distance limit of $\{U, F, V_s, V_w\}$ as shown in Fig. 1. Note that the light parton masses from the quasiparticle fit are different from the results extracted using the off-shell many-body calculations [16], while the charm-quark masses of $\{V_s, V_w\}$ are taken from the corresponding potential. This setup allows for an approximate "apples-to-apples" comparison of how the different forces (or "effective couplings") shown in Figs. 2, 3 and 4 manifest themselves in the charm-quark transport coefficients.

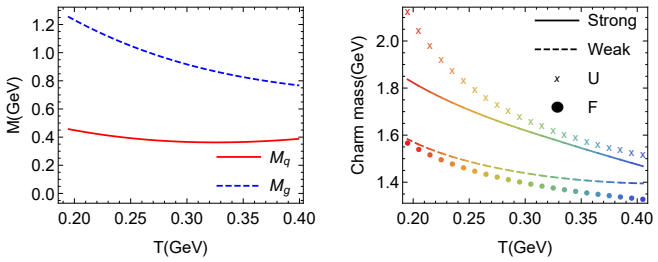


FIG. 5. Light-parton (left) and charm-quark (right) masses for V_s (solid lines), V_w (dashed lines), U (crosses) and F (dots) as used in the quasiparticle calculations leading to the results displayed in Figs. 8.

We start with the case of using the Born approximation to calculate the friction coefficient, displayed in Fig. 6 for the four potentials. The results for the WCS potential and the free energy closely agree across all temperatures and charm-quark momenta considered here. The friction coefficient is much larger for the SCS potential and the internal energy, which are also rather close to each other except that the U-potential is about a factor 2 larger at the lowest temperature and at high momenta at the highest temperature.

To better understand what the relevant momentum exchanges for the transport coefficients are, we divide

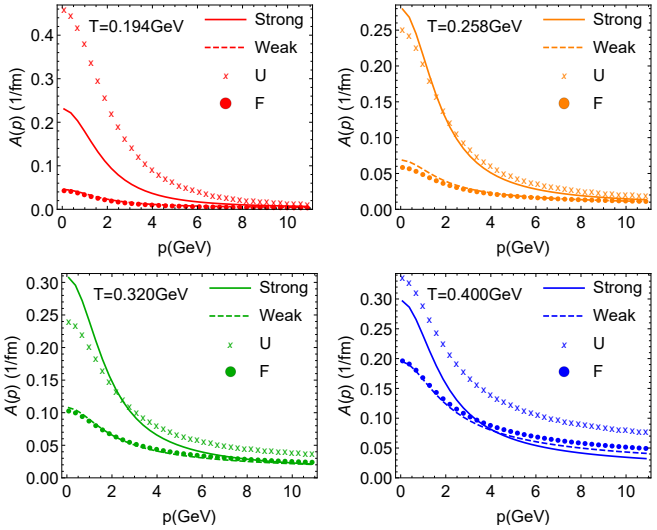


FIG. 6. Friction coefficients for V_s (solid line), V_w (dashed line), U (crosses) and F (dots) when using the on-shell Born diagrams in quasiparticle approximation.

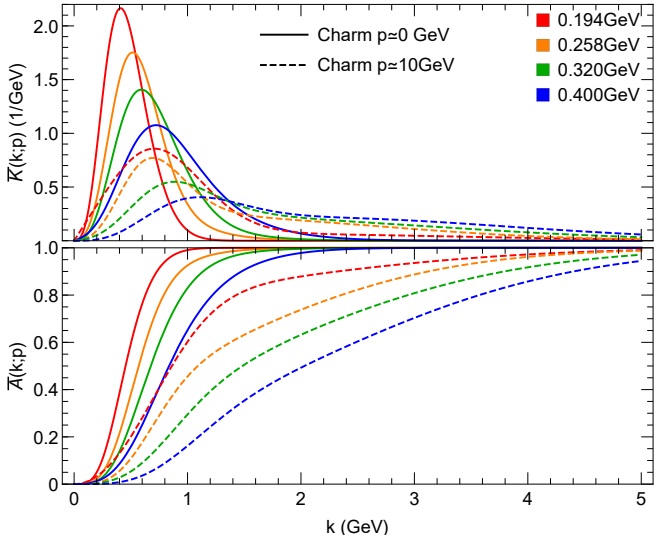


FIG. 7. Differential CM momentum-transfer "probability" distribution, $\bar{K}(k;p)$ (upper panel), for the friction coefficient from the SCS potential in Born approximation, and its cumulative (lower panel) for charm quarks at zero momentum (p=0, solid lines) and p=10 GeV (dashed lines) for different temperatures (identified by the color code).

up the phase space into shells of momentum transfer, kdk, where $k = |\vec{p}_{\rm cm} - \vec{p}'_{\rm cm}|$, and define a "normalized" momentum-exchange density

$$\bar{K}(k;p)dk \equiv A(p)^{-1}dA(k) \tag{16}$$

and a corresponding cumulative density

$$\bar{A}(k;p) \equiv \int_0^k dk' \bar{K}(k';p) \tag{17}$$

of the friction coefficient, $A(p)$, defined such that $\bar{A}(p, k \to \infty)$=1. These two quantities are plotted in Fig. 7 using the SCS potential, V_s (still in quasiparticle and Born approximation). For low-momentum charm quarks, most of the momentum transfers at low temperatures occur in a 0.5 GeV window around k=0.4 GeV, corresponding to a relatively large force range of ∼1 fm (recall the remark at the end of Sec. II). The peak position shifts to higher momentum transfer as temperature or HQ momentum increase, implying a transition from the long-range string force to a shorter-range Coulomb force. This is due to a harder thermal phase space and the enhanced screening of the potential as temperature increases. For the U potential, the effective coupling at a momentum exchange of ∼0.5 GeV is about 50% larger at the lowest temperature (recall upper left panel in Fig. 4), leading to an approximately twice larger low-momentum friction coefficient in Fig. 6. A similar analysis applies to the other potentials.

In the next step, we compare the friction coefficients from the resummed T-matrix interactions in Fig. 8, still using a quasiparticle QGP medium. At low temperature and low momentum, the drag coefficients for U and V_s are *reduced* by a factor of 2 and 1.5, respectively, compared to the Born calculation. This is mainly because

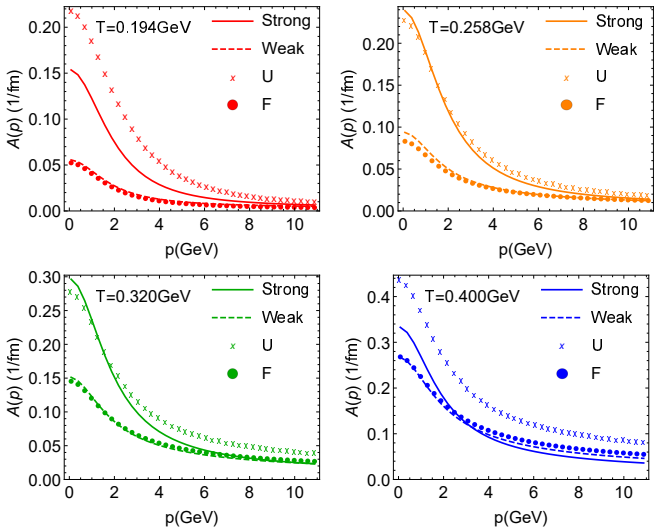


FIG. 8. Quasiparticle friction coefficients for V_s (solid line), V_w (dashed line), U (crosses) and F (dots).

the resummation converts the strongly attractive Born term into subthreshold resonance states whose interaction strength is not accessible in 2→2 on-shell scattering, while only a repulsive tail of the T-matrix remains in the on-shell phase space. However, for a less attractive potential which does not generate a strong bound state, which is the case for F and V_w, the resummation generally enhances the Born result. On the other hand, at high momentum and high temperature, a closer agreement between the Born approximation and T-matrix results is found.

B. Transport coefficients with off-shell effects

In the previous section we saw how in a strongly coupled medium the formation of bound states can lead to a marked *decrease* in the interaction strength when employing the quasiparticle approximation in two-body scattering. This should be considered as an artifact of an incompatible approximation. In the presence of a large interaction strength, the single-particle spectral functions are expected to become broad and/or develop collective modes below their nominal "quasiparticle" masses. In either case, phase space opens up below the quasiparticle two-body threshold and allows for subthreshold resonance scattering. We now compute the charm-quark transport coefficients deploying the off-shell formalism described in Sec. III to incorporate the quantum effects associated with subthreshold many-body interactions. We focus on the results for the SCS and WCS as their selfconsistent solutions constructed in Ref. [16] specify the spectral functions of the thermal partons, while this information is not available for U nor F.

The pertinent charm-quark friction coefficients are compiled in Fig. 9. The full results displayed in the upper left panel show that for small momenta and small temperatures the relaxation rate is about four times larger for the SCS than for the WCS, while with increasing momentum and temperature they approach each other. The key reason for the large enhancement at low momentum and temperature is the remnant of the long-range confining force, as discussed in the context of Figs. 1, 2, 3 and 4. At higher temperatures, the confining potential is largely screened, and the larger thermal parton momenta probe the force at shorter distances. Since the short-range Coulomb force is quite similar for the WCS and SCS, the difference between $A_s(p)$ and $A_w(p)$ is reduced (in the fits of Ref. [16] the screening of the Coulomb interaction is slightly weaker in the WCS than in the SCS, causing $A_w(p)$ to exceed $A_s(p)$ at high momenta and at the highest temperature where the confining interaction has nearly vanished).

The off-shell effects in the SCS scenario are illustrated in the middle and right panel of Fig. 9, where we have switched them off for either both thermal partons and the outgoing charm quark (middle panel) or only for the outgoing charm quark (right panel). In the former case, we have re-adjusted (*i.e.*, decreased) the thermal parton masses to ensure compatibility with the lQCD EoS. We find that the quantum effects almost double the transport coefficients in the small-momentum and low-temperature region: the broadening of the thermal spectral functions allows to probe off-shell energies in the T-matrix where scattering through a (broad) bound state becomes possible. This confirms, in a more rigorous treatment, the original findings of Refs. [20, 21], where near threshold resonances were put forward to solve the heavy-flavor puzzle in Au-Au collisions at RHIC [22]. A more moderate but still significant effect arises from the non-trivial spectral function of the outgoing charm quark. Switching back to a δ-function reduces the low-momentum low-temperature relaxation rate by almost 20%, cf. right panel of Fig. 9. Once the resonance states are close to threshold (or have melted) so that the on-shell treatment can already access the main scattering strength, the off-shell treatment does not provide a significant enhancement. For the WCS, the results from the full off-shell case generally agree well with the results from the quasiparticle case (not shown), since the widths of spectral functions are small. At high momentum, the HQ drag coefficients are dominated by the Coulomb term, augmented by relativistic (magnetic) corrections (Breit enhancement), while the scalar vertex assumed for the string interaction suppresses its high-momentum contribution. Therefore, the off-shell case approaches the quasiparticle case: the spectral functions become more quasiparticle like, and the typical CM energy in the T-matrix becomes larger so that even off-shell effects do not significantly probe the subthreshold resonances anymore.

In Fig. 10 we summarize the temperature dependence of the zero-momentum relaxation rate, $\gamma = A(p \to 0)$, and the dimensionless spatial diffusion coefficient, $D_s(2\pi T) = (2\pi T^2)/(m_c\gamma_c)$, for the WCS and SCS. As a reference, we also show a perturbative QCD (pQCD) Born result (using α_s=0.4 in a quasiparticle QGP with Debye and thermal parton masses of gT, and a constant charm-quark mass of 1.5 GeV) upscaled by a factor of 5 (as recently used as a benchmark scenario in Ref. [23]). The temperature behavior of the relaxation rates and spatial diffusion coefficients for the WCS is similar to the pQCD*5 scenario, wherein γ increases monotonically with temperature and $D_s(2\pi T)$ is essentially constant, similar to what one would expect from a dimensionless theory. For the SCS, on the other hand, γ exhibits a rather flat behavior with temperature where the increasing density of the thermal scatterers is essentially compensated by the decreasing interaction strength. Consequently, $D_s(2\pi T)$ increases with temperature by about a factor 5 over the considered temperature range of T=0.2-0.4 GeV; the extra dimensionful quantity is brought in by the nonperturbative string tension. Also note that the SCS diffusion coefficient differs from the "bare" pQCD interaction by a factor of almost 15 at low temperature.

C. Scrutinizing Nonperturbative Effects

In the calculation of the transport coefficients, there are at least three nonperturbative components: (1) the string interaction in the potential; (2) the resummation of the T-matrix possibly leading to the resonance formation; (3) off-shell effects from the large widths of the partons. Here, we reassess these effects relative to the full calculation of the friction coefficient within the SCS in Fig. 11, using the thermal parton and charm-quark masses shown in Fig. 5.

When switching off the string interaction in the potential (and neglecting off-shell effects, which play a neg-

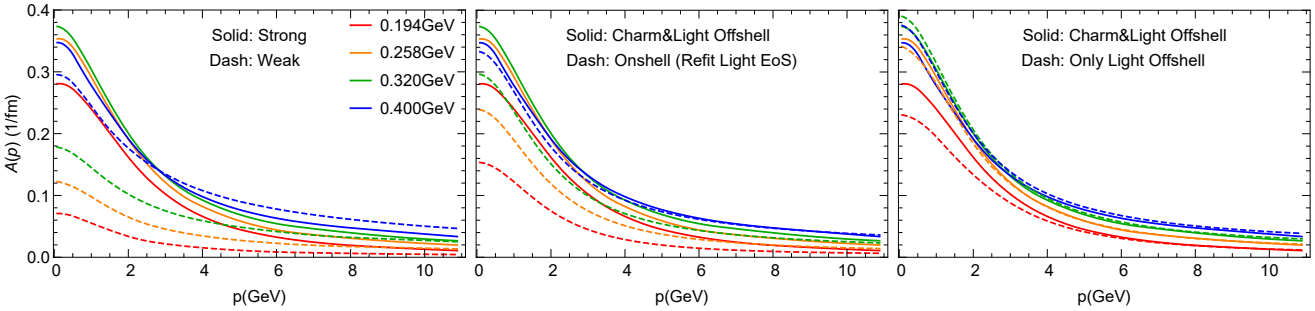


FIG. 9. Charm-quark friction coefficients, $A(p)$, for the full off-shell calculations (left) in the SCS (solid lines) and WCS (dashed lines), and comparing the full off-shell case for the SCS (solid lines) with one using the on-shell approximation for both thermal partons and the outgoing charm quark (dashed lines; middle panel) or for the outgoing charm quark only (dashed lines in right panel).

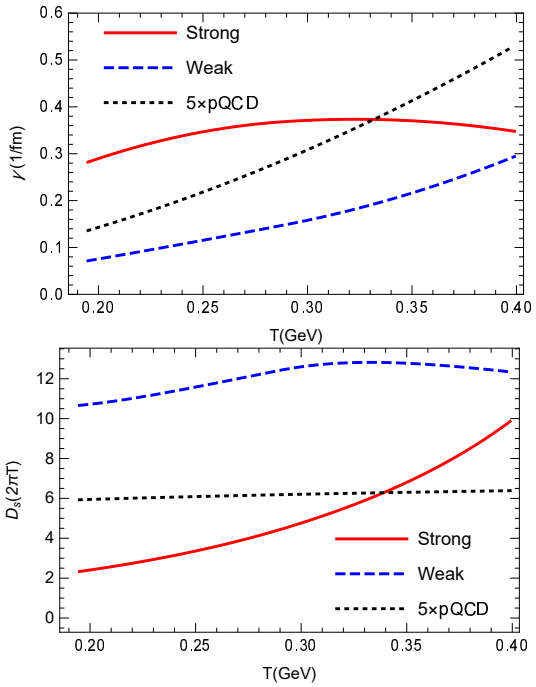


FIG. 10. Temperature dependence of the zero-momentum relaxation rate, γ (upper), and the spatial diffusion coefficient, $D_s = T/(\gamma M_c)$ (lower, in units of the thermal wave length $D_s(2\pi T)$). The pQCD results uses α_s =0.4 and a factor of 5.

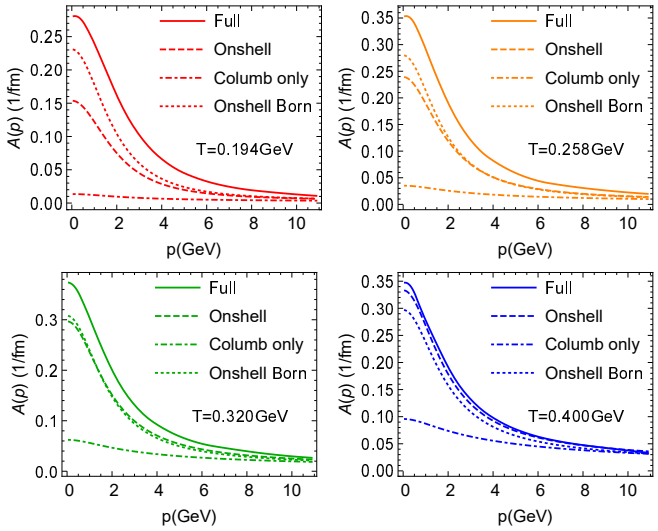


FIG. 11. Comparison of the effects of different ingredients on the HQ transport coefficients in the SCS as a function of charm-quark momentum, at 4 different temperatures. Solid lines: full results; dashed lines: using the on-shell approximation for the thermal partons and outgoing charm-quark; dash-dotted line: on-shell results using only the Coulomb term in the potential; dotted lines: using the Born and quasiparticle approximation (including the confining potential).

ligible role in this scenario), the pertinent T-matrix results for the friction coefficient (labeled "Coulomb-only" in Fig. 11) are much reduced compared to the full results at low momentum, close to a factor of 15 at low temperature, and still by a factor of ∼3 at T=0.4 GeV. At charm-quark momenta of p=10 GeV, the reduction is still significant at low T (indicating a non-negligible portion of soft interactions driven by the string term), but has essentially ceased at T=0.4 GeV. Therefore, perturbative (elastic) calculations of $A(p)$ that do not account for remnants of the confining term are not be reliable at low temperatures even at momenta of p = 10 GeV. The "on-shell" results with the full interaction, already shown in the previous section, fall below the full results by almost 50% at low T and nearly uniform in 3-momentum from 0 to 10 GeV. This implies that even at p=10 GeV, the soft off-shell effects (making accessible the subthreshold resonances) are significant, although in practice one expects radiative processes to become dominant at these momenta. The difference between full and on-shell calculations is essentially gone at T=0.4 GeV (resonance structures have ceased), again basically across the entire momentum range. Finally, the "on-shell Born" results are surprisingly close to full results within a few 10's of percent. This is, however, a highly deceptive result: if we include the second Born term in the T-matrix, the friction coefficient is up to 5 times larger at low momentum and

low temperature, signaling an uncontrolled convergence property of the perturbative series at low momentum, very similar to the findings in Ref. [24]. This is another reminder that a proper resummation in the nonperturbative region is mandatory. Figure 11 furthermore shows that the "on-shell Born" and "on-shell" curves approach each other at high momentum. Still, the results for the second Born order at high momentum and low temperature double the first-order result, *i.e.*, the convergence of the perturbative series is still not good (due to the presence of the string term). This situation improves at higher temperature: at T =0.4 GeV, the second Born contribution is only by a factor 1.8 (1.6) larger than the Born contribution at low (high) momentum.

V. CHARM-QUARK LANGEVIN SIMULATIONS IN HEAVY-ION COLLISIONS

In this section we implement the transport coefficients following from the selfconsistent WCS and SCS, as well as from the U-potential proxy with quasiparticle QGP medium, into Langevin simulations of charm quarks in URHICs as described in Ref. [25]. As our current calculations are limited to temperatures T=0.194-0.4 GeV and momenta p=0-10 GeV, an extrapolation is required to cover the ranges needed in the Langevin approach to heavy-ion collisions at the LHC. Since the p-dependence of the quasiparticle results is similar to the full results at high momentum (as discussed in the previous section), we extrapolate $A(p)$ to higher momenta using the quasiparticle results augmented by a p-independent K factor to smoothly connect them at p=10 GeV. For the extrapolation to lower and higher temperatures, we first extrapolate $D_s(2\pi T)$ and m_c as shown in the lower two panels of Fig. 12. Then, we use $A(p=0;T)=T/(D_s m_c)$ and take the momentum dependence of $A(p;T)$ to be the same as for $A(p;T)$ at T=0.194(0.4) GeV for low (high) temperature, as shown in the upper two panels of Fig. 12.

The transport coefficients are utilized within the Langevin equations

$$d\mathbf{x} = \frac{\mathbf{p}}{\varepsilon_c(p)} dt \tag{18}$$

$$d\mathbf{p} = \Gamma(p)\,\mathbf{p} dt + \sqrt{2dtD(p)}\boldsymbol{\rho}\ , \tag{19}$$

where the relaxation rate, $\Gamma(p)$, and the momentum diffusion coefficient, $D(p)$, are taken to be $\Gamma(p)=A(p)$ and $D(p)=B_0(p)=B_1(p)=T\varepsilon_c(p)\Gamma(p)$, and $\boldsymbol{\rho}$ is a random number determined from the Gaussian distribution function $P(\boldsymbol{\rho}) = (2\pi)^{-3/2}e^{-\boldsymbol{\rho}/2}$. Using the Langevin equations, we simulate Brownian motion of charm quarks in a background medium provided by an ideal hydrodynamic evolution of the QGP fireball in URHICs at RHIC and the LHC. For definiteness, we choose semicentral Pb-Pb collisions at CM energy $\sqrt{s_{\rm NN}}$=5.02 TeV, at a fixed impact parameter representing the 20-40% centrality class.

Figure 13 summarizes the nuclear modification factor, $R_{\rm AA}$, and elliptic flow, v_2, of charm quarks at the end of

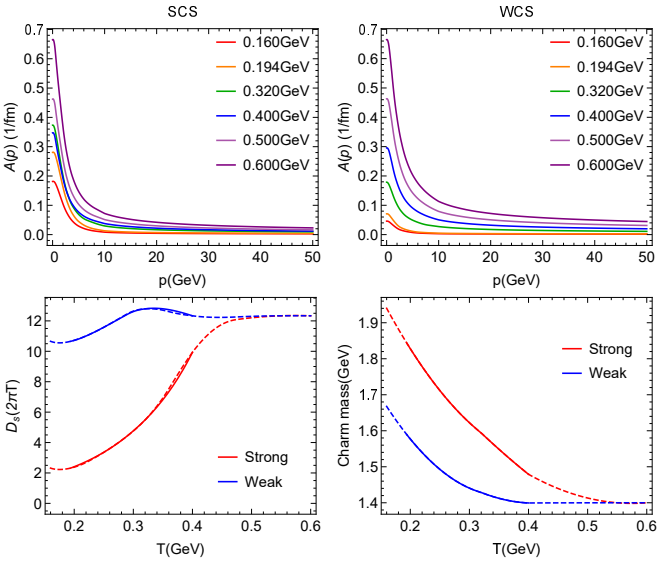


FIG. 12. Extrapolation results for $D_s(2\pi T)$, M_c, $A_s(p)$ and $A_w(p)$.

the QGP evolution, taken at $T_{\rm pc}$=170 MeV, for the three potentials under investigation. The $R_{\rm AA}$ shows the standard feature of softening the initial charm-quark spectra, but only exhibits a modest sensitivity to the underlying potential. This reiterates the finding [26] that the main effects determining the charm-quark $R_{\rm AA}$ occur early in the evolution where the difference between the potentials is small. This is quite different for the elliptic flow [26], which requires several fm/c to build up in the expanding fireball. At that point the difference in the underlying potential scenarios becomes maximal, and, consequently, the low-p_t elliptic flow of charm quarks provides a direct gauge of the coupling strength in the later stages of the QGP evolution. More quantitatively, the largest value of the v_2 is generated within the SCS reaching near 10%, more than a factor of 3 larger than in the WCS. It also exceeds the maximum value attained with the U-potential proxy by about 20%, indicating that low-p_t elliptic flow of charm quarks is rather sensitive to the long-distance behavior of the in-medium potential, and thus an excellent measure of the spatial diffusion coefficient. Note that a charm-quark momentum of p_t=2 GeV corresponds to a velocity of about 0.74c, not much larger than the (surface) flow velocities reached in the fireball expansion at the end of the QGP phase. At higher p_t, above ∼4 GeV, the intermediate-distance strength is largest in the U-potential and leads to significantly larger v_2 values than obtained for V_s and V_w.

To make contact with experiment, we proceed to calculate D-meson observables. As the fireball medium approaches the pseudo-critical temperature, charm quarks are hadronized into D mesons through either recombination with surrounding light quarks from the hydrodynamic medium (pre-dominantly at low p_t) [27] or independent fragmentation (we also account for a ∼20%

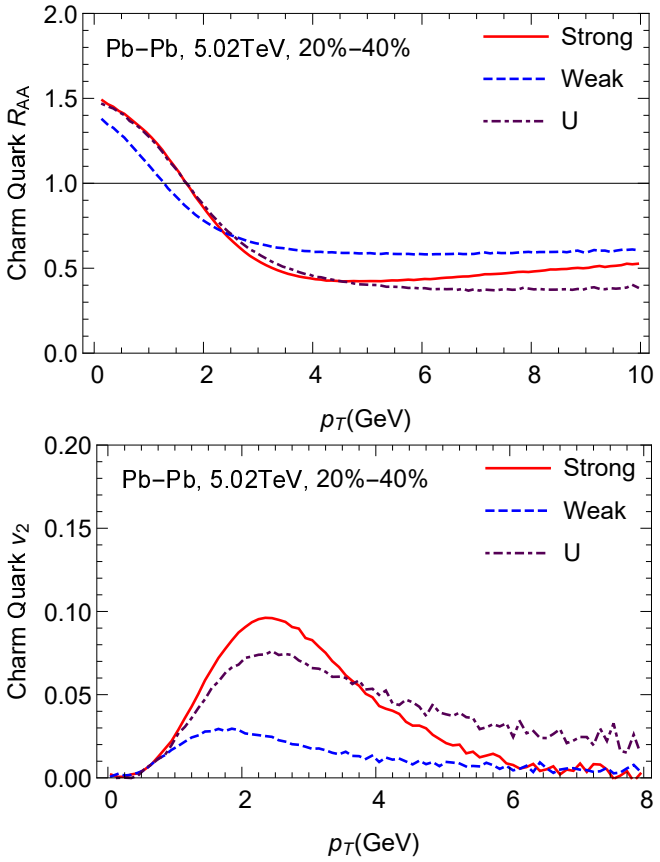


FIG. 13. The $R_{\rm AA}$ (upper panel) and v_2 (lower panel) of charm quarks calculated from the T-matrix interactions with 3 different potentials using relativistic Langevin simulations in a hydrodynamic fireball evolution for semicentral Pb-Pb collisions at the LHC.

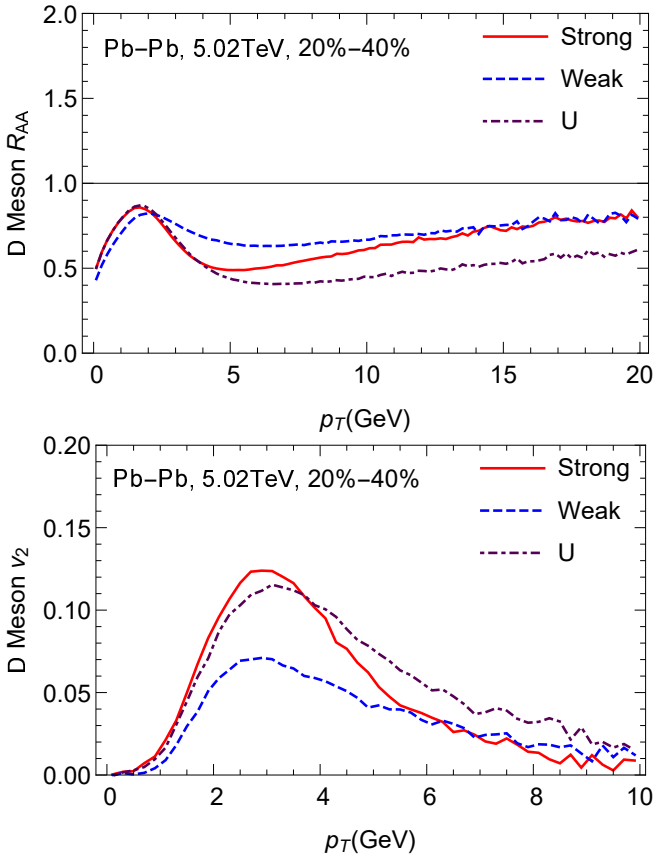


FIG. 14. Comparison of the calculated D-meson $R_{\rm AA}$ (upper panel) and v_2 (lower panel) obtained from applying a recombination-fragmentation model to hadronize the charm-quark spectra plotted in Fig. 13.

(p_t-dependent) reduction in the D-meson yields due to shadowing and "chemistry effects" where charm quarks hadronize into other hadrons like D_s and Λ_c at a higher fraction than in proton-proton collisions). We finally carry out the D-meson diffusion in the hadronic phase. The resulting D-meson $R_{\rm AA}$ and v_2 are shown in Fig. 14. Recombination effectively acts as another interaction between charm quarks and the medium, driving the D-meson spectra closer to equilibrium [25]. This produces a characteristic flow "bump" in the $R_{\rm AA}$ at a p_T reflecting the velocity of low-momentum D-mesons embedded in the flowing hydrodynamic medium. At high p_T, fragmentation takes over, and the D-meson $R_{\rm AA}$ tends toward that of the charm quark (modulo further suppression due to D-meson interactions in the hadronic phase). Other than the flow bump, the qualitative features of the charm-quark spectra relating to the different potentials are preserved at the D-meson level. However, the discrimination power is reduced, especially for the maximum value of the v_2, which is now quite similar for the SCS and the U-potential, while the v_2 of the WCS is only a factor 2 below the former two. This is because recombination plus hadronic diffusion together add a roughly equal amount of v_2 in the 3 potential scenarios when going from charm-quark to D-meson spectra. To some extent this is an artifact of applying the same coalescence model to all three scenarios. In reality, the coalescence probability should be smaller in the WCS compared to the SCS, since the D-meson resonance strength, which is the microscopic mediator of the recombination process, is weaker in the WCS than in the SCS and thus should lead to a smaller increment in v_2 in the former compared to the latter. While the resonance recombination model [27] (as employed here) in principle encodes this mechanism, its implementation in the current calculation does not account for this difference. These considerations reiterate the importance of a recombination model that is consistent with the microscopic interactions driving the diffusion process in the the vicinity of $T_{\rm pc}$.

Recalling the experimental results [28–30], which report maximal v_2 values of D-mesons in 30-50% central collision of ca. 17±2%, the SCS scenario is not far below, but the WCS and also the free-energy potential (not shown here) are strongly disfavored as their interaction strength is too small. At higher momenta, $p_T \gtrsim 5\,$GeV, both WCS and SCS produce too little suppression and too little v_2 (even the U potential did not supply enough

suppression in comparisons to central Pb-Pb data). This is, however, expected, since radiative processes have not been systematically included yet (some are encoded through the in-medium selfenergies of the heavy and light quarks in the T-matrices), see, *e.g.*, Ref. [23] for a recent discussion and references. Such processes may also help to reduce the milder discrepancies at lower p_T. It remains to be seen whether contributions beyond the potential approximation might be helpful in generation additional interaction strength. From a more practical perspective, fluctuating initial conditions in the hydrodynamic evolution are conceivable for producing an enhancement in the v_2 over the results from smooth initial conditions [31–34] as employed in the ideal hydrodynamic evolution used here.

VI. CONCLUSIONS AND PERSPECTIVES

In an attempt to establish connections between heavy-flavor phenomenology in heavy-ion collisions and the microscopic interactions driving the diffusion of heavy quarks through the QGP formed in these reactions, we have employed a range of underlying two-body interaction potentials to compute the heavy-light T-matrices and pertinent HQ transport coefficients. Specifically, we have investigated two potentials recently constructed to satisfy constraints from lQCD for HQ free and internal energies, quarkonium correlators and the QGP EoS, as well as the free and internal energies, which have been used previously as potential proxies. We have first analyzed the corresponding forces, in particular their typical ranges in both coordinate and momentum space. As expected, the U-potential yields the largest force strength, realized at intermediate distances, while the strongly coupled T-matrix solution develops a smaller force but of longer range; in both cases the remnants of the confining force in the QGP play a key role in generating nonperturbative interaction strength, operative for temperatures of up to about $2.5\,T_{\rm pc}$. The weakly coupled solution and the free energy have very similar forces, but are further reduced in strength and of much shorter range than the internal energy and the strongly coupled solution. We then derived a transport equation including quantum many-body (off-shell) effects, to account for the broad spectral functions of the thermal medium partons characterizing, in particular, the SCS of the T-matrix solution. These off-shell effects are instrumental in enabling the diffusing heavy quarks to probe the interaction strength of the broad subthreshold two-body resonances in the heavy-light scattering amplitudes. As a somewhat surprising result, the SCS potential develops the largest thermal relaxation rate for low-momentum charm quarks among all four potentials, while the U-potential's rate is strongest at intermediate and large momenta. Implementing these potentials into relativistic Langevin simulations revealed the SCS potential to develop the largest peak value of the charm-quark v_2, about 20% above the U-potential and a factor of 3 larger than the WCS potential (or free energy). Computing pertinent D-meson observables and benchmarking them against experimental data at the LHC rules out the WCS and free energy as viable potentials for HQ interactions in the QGP. Even the SCS potential falls slightly short of accounting for the existing low-momentum v_2 data at the LHC. These findings imply that charm quarks acquire collisional widths of 0.5-1 GeV in the QGP near $T_{\rm pc}$, and consequently low-momentum light partons are likely dissolved in this regime, *i.e.*, soft excitations in the QGP near $T_{\rm pc}$ do not support parton quasiparticles; at the same time, broad hadronic resonances emerge and act as mediators of the nonperturbative interaction strength.

Among the challenges that remain in the HQ sector, from a microscopic point of view, are to account for the missing 20% in the elliptic flow of D-mesons as observed at the LHC, and to incorporate gluon radiation in a strongly-coupled framework. The latter will be essential to increase the high-p_T suppression and v_2, whereas genuine 3-body scattering, retardation effects, improvements in the coalescence mechanism and/or the hadronic diffusion, as well as features of the bulk evolution not captured by the ideal-hydro model employed here, could augment the v_2 at low-p_T. Work on several aspects of the above has already been done by various groups and/or is in progress, and efforts to combine them are ongoing [23] and expected to reveal further insights in due course.

ACKNOWLEDGMENTS

This work was supported by the U.S. National Science Foundation (NSF) through grant PHY-1614484, by the A.-v.-Humboldt Foundation, and by the NSFC grant 11675079.

Appendix A: Center-of-Mass Transformation

In this appendix, we provide details on the CM transformation implemented in this work. We first discuss the CM transformation in a nonrelativistic system, followed by the relativistic case.

The nonrelativistic T-matrix can be expressed as

$$T(E,\mathbf{P},\mathbf{p}_1,\mathbf{p}_1') = V(\mathbf{p}_1-\mathbf{p}_1')+ \int_{-\infty}^{\infty}\frac{d^3\mathbf{k}_1}{(2\pi)^3}V(\mathbf{p}_1-\mathbf{k}_1)G_{(0)}^{(2)}(E,\mathbf{k}_1,\mathbf{P}-\mathbf{k}_1)T(E,\mathbf{P},\mathbf{k}_1,\mathbf{p}_1'). \tag{A1}$$

where the total 3-momentum and energy are $\mathbf{P}=\mathbf{p}_1+\mathbf{p}_2$ and $E=\omega_1+\omega_2+i\epsilon$, respectively. In a nonrelativistic system, the two-body propagator reads

$$G_{(0)}^{(2)}(E,\mathbf{k}_1,\mathbf{P}-\mathbf{k}_1) = \frac{1}{E-\frac{\mathbf{k}_1^2}{2M_1}-\frac{(\mathbf{P}-\mathbf{k}_1)^2}{2M_2}}\,, \tag{A2}$$

and the CM transformation can be expressed as

$$\mathbf{v}_{\rm cm} = \frac{\mathbf{P}}{M_{\rm tot}} \ , \tag{A3}$$

$$\mathbf{p}_{\rm cm} = \mathbf{p} - M_i \mathbf{v}_{\rm cm} \ , \tag{A4}$$

where $\mathbf{p}$ (and the corresponding $\mathbf{p}_{\rm cm}$) is a generic notation for $\mathbf{p}_{1,2}, \mathbf{p}'_{1,2}, \mathbf{k}_1$, etc., and $M_{\rm tot} = M_1 + M_2$ is the total mass. Therefore, the transformations for the momenta are $\mathbf{p}_1 = \mathbf{p}_{\rm cm} + M_1 \mathbf{v}_{\rm cm}, \mathbf{p}'_1 = \mathbf{p}'_{\rm cm} + M_1 \mathbf{v}_{\rm cm}, \mathbf{k}_1 = \mathbf{k}_{\rm cm} + M_1 \mathbf{v}_{\rm cm}$. Substituting these into Eq. (A1) and noting that $V(\mathbf{p}_1 - \mathbf{p}'_1) = V(\mathbf{p}_{\rm cm} - \mathbf{p}'_{\rm cm})$, we obtain an equivalent equation that only depends on E and $\mathbf{P}$ implicitly through $E_{\rm cm} = E - \mathbf{P}^2/(2M_{\rm tot})$,

$$T(E_{\rm cm}, \mathbf{p}_{\rm cm}, \mathbf{p}'_{\rm cm}) = V(\mathbf{p}_{\rm cm} - \mathbf{p}'_{\rm cm}) + \int_{-\infty}^{\infty} \frac{d^3\mathbf{k}_{\rm cm}}{(2\pi)^3} V(\mathbf{p}_{\rm cm} - \mathbf{k}_{\rm cm}) \frac{1}{E_{\rm cm} - \frac{(\mathbf{k}_{\rm cm})^2}{2\mu}} T(E_{\rm cm}, \mathbf{k}_{\rm cm}, \mathbf{p}'_{\rm cm}) \ , \tag{A5}$$

with the reduced mass $\mu = M_1 M_2 / M_{\rm tot}$. The solution to the original equation (A1) is calculated using the reverse CM transformation,

$$\mathbf{p}_{\rm cm} = \mathbf{p}_1 - \frac{M_1 \mathbf{P}}{M_{\rm tot}} = \frac{\mathbf{p}_1 M_2 - \mathbf{p}_1 M_1}{M_{\rm tot}}$$

$$\mathbf{p}'_{\rm cm} = \mathbf{p}'_1 - \frac{M_1 \mathbf{P}}{M_{\rm tot}} = \frac{\mathbf{p}'_1 M_2 - \mathbf{p}'_1 M_1}{M_{\rm tot}} \ . \tag{A6}$$

In vacuum, solving the equation in the CM frame and transforming back to an arbitrary frame results in the same solution as obtained from solving the original equation, due to Galilean invariance. No approximations are necessary in this procedure. In medium, neglecting the blocking factor and using the two-body selfenergy [16] to include medium effects, the T-matrix equation in the the-body CM frame is given by

$$T(E_{\rm cm}, \mathbf{p}_{\rm cm}, \mathbf{p}'_{\rm cm}) = V(\mathbf{p}_{\rm cm} - \mathbf{p}'_{\rm cm}) + \int_{-\infty}^{\infty} \frac{d^3\mathbf{k}_{\rm cm}}{(2\pi)^3} V(\mathbf{p}_{\rm cm} - \mathbf{k}_{\rm cm}) \times \frac{1}{E_{\rm cm} - \frac{(\mathbf{k}_{\rm cm})^2}{2\mu} - \Sigma^{(2)}(E, \mathbf{P}, \mathbf{k}_{\rm cm})} T(E_{\rm cm}, \mathbf{k}_{\rm cm}, \mathbf{p}'_{\rm cm}) \ . \tag{A7}$$

Here, the CM approximation assumes that the two-body selfenergy only depends on $\mathbf{P}$ and E through $E_{\rm cm}$, so that $\Sigma^{(2)}(E, \mathbf{P}, \mathbf{k}_{\rm cm}) \approx \Sigma^{(2)}(E_{\rm cm}, 0, \mathbf{k}_{\rm cm}) \equiv \Sigma^{(2)}(E_{\rm cm}, \mathbf{k}_{\rm cm})$. The CM transformations have the same form in medium and in vacuum, but it is an approximation for the in-medium case. Thus, the CM transformation can be understood as expressing $\mathbf{p}_{\rm cm}$ as a function of $\{M_1, M_2, \mathbf{p}_1, \mathbf{p}_2\}$ and $\mathbf{p}'_{\rm cm}$ as a function of $\{M'_1, M'_2, \mathbf{p}'_1, \mathbf{p}'_2\}$. This is the motivation for defining and analogous transformation for the relativistic in-medium off-shell case.

In the relativistic case, transformations to an arbitrary frame are Lorentz transformations (with $\parallel$ and $\perp$ indicating parallel and perpendicular to the relative velocity, respectively),

$$\varepsilon'_p = \gamma(\varepsilon_p - v p_\parallel) \ , \ p'_\parallel = \gamma(p_\parallel - v\varepsilon_p) \ , \ \mathbf{p}'_\perp = \mathbf{p}_\perp$$

$$p_\parallel = \mathbf{p} \cdot \hat{\mathbf{v}} \ , \ \mathbf{p}_\perp = \mathbf{p} - p_\parallel \hat{\mathbf{v}}, \tag{A8}$$

where $\hat{\mathbf{v}}$ denotes the unit vector in the direction of the velocity. Relativistic CM transformations, in analogy to Eq. (A6), are realized using the quantities

$$\mathbf{v}_{\rm cm} = \frac{\mathbf{p}_1 + \mathbf{p}_2}{\varepsilon_{\rm p_1} + \varepsilon_{\rm p_2}} \tag{A9}$$

$$\gamma_{\rm cm} = \frac{\varepsilon_{\rm p_1} + \varepsilon_{\rm p_2}}{\sqrt{s}} \tag{A10}$$

$$s = (\varepsilon_{\rm p_1} + \varepsilon_{\rm p_2})^2 - (\mathbf{p}_1 + \mathbf{p}_2)^2 \ . \tag{A11}$$

After obtaining the T-matrix solution in the CM frame, it is necessary to express $\{E_{\rm cm}, \mathbf{p}_{\rm cm}, \mathbf{p}'_{\rm cm}\}$ in terms of $\{\mathbf{p}_1, \mathbf{p}_2, \mathbf{p}'_1, \mathbf{p}'_2, E\}$ to obtain the solution in an arbitrary frame. The relativistic CM transformation for energy is simply $\sqrt{s} \equiv E_{\rm cm} = \sqrt{E^2 - P^2}$. For the a CM 3-momentum, $\mathbf{p}_{\rm cm}$, it can be expressed in terms of components parallel and perpendicular to $\mathbf{v}_{\rm cm}$ as

$$p_{\rm cm\parallel} = \gamma_{\rm cm}(p_\parallel - v_{\rm cm}\varepsilon_p) = \frac{\varepsilon_{\rm p_2} p_{1\parallel} - \varepsilon_{\rm p_1} p_{2\parallel}}{\sqrt{s}}$$

$$\mathbf{p}_{\rm cm\perp} = \mathbf{p}_\perp = \mathbf{p} - p_\parallel \hat{\mathbf{v}}_{\rm cm} = \frac{\mathbf{p}_1 p_{2\parallel} - \mathbf{p}_2 p_{1\parallel}}{|\mathbf{p}_1 + \mathbf{p}_2|} \ , \tag{A12}$$

and likewise for primed momenta, together with the constraint on total momentum conservation, $\mathbf{p}_1 + \mathbf{p}_2 = \mathbf{p}'_1 + \mathbf{p}'_2$. The CM transformation for $p_{\rm cm} = |\mathbf{p}_{\rm cm}|$, $p'_{\rm cm} = |\mathbf{p}'_{\rm cm}|$, and $\cos(\theta_{\rm cm}) = \mathbf{p}_{\rm cm} \cdot \mathbf{p}'_{\rm cm} / (p_{\rm cm} p'_{\rm cm})$ in Eq. (15) can be obtained using Eq. (A12) and its primed counterpart. The Galilean CM transformations are recovered in the nonrelativistic limit. In the on-shell limit, the relativistic CM transformation used in Ref. [9] is recovered. However, since the transformation introduced here does not involve the external energies, the analytical properties of the transformed T-matrix are preserved more accurately, while in the prescription of Ref. [9] the Lorentz invariance of the Mandelstam variables is preserved. Since our focus here is on the low-momentum properties of the heavy quarks, in connection with off-shell effects, we choose as our default is the new prescription of Eq. (A12). In practice, the imaginary parts of the parton selfenergies calculated within the present prescription tend to be 10% larger at their peak values compared to the previous prescription used in Ref. [9].

[1] P. Petreczky and K. Petrov, Phys. Rev. D **70**, 054503 (2004).

[2] O. Kaczmarek and F. Zantow, Phys. Rev. D **71**, 114510

(2005).
[3] S. Borsanyi, Z. Fodor, C. Hoelbling, S. D. Katz, S. Krieg, C. Ratti, and K. K. Szabo (Wuppertal-Budapest), JHEP **09**, 073 (2010).
[4] A. Bazavov *et al.*, Phys. Rev. D **85**, 054503 (2012).
[5] C.-Y. Wong, Phys. Rev. C **72**, 034906 (2005).
[6] D. Cabrera and R. Rapp, Phys. Rev. D **76**, 114506 (2007).
[7] W. M. Alberico, A. Beraudo, A. De Pace, and A. Molinari, Phys. Rev. D **75**, 074009 (2007).
[8] A. Mocsy and P. Petreczky, Phys. Rev. D **77**, 014501 (2008).
[9] F. Riek and R. Rapp, New J. Phys. **13**, 045007 (2011).
[10] A. Jakovac, P. Petreczky, K. Petrov, and A. Velytsky, Phys. Rev. D **75**, 014506 (2007).
[11] G. Aarts, C. Allton, M. B. Oktay, M. Peardon, and J.-I. Skullerud, Phys. Rev. D **76**, 094513 (2007).
[12] H. T. Ding, A. Francis, O. Kaczmarek, F. Karsch, H. Satz, and W. Soeldner, Phys. Rev. D **86**, 014509 (2012).
[13] G. Aarts, C. Allton, T. Harris, S. Kim, M. P. Lombardo, S. M. Ryan, and J.-I. Skullerud, JHEP **07**, 097 (2014).
[14] M. Mannarelli and R. Rapp, Phys. Rev. C **72**, 064905 (2005).
[15] S. Y. F. Liu and R. Rapp, (2016), arXiv:1612.09138 [nucl-th].
[16] S. Y. F. Liu and R. Rapp, Phys. Rev. C **97**, 034918 (2018).
[17] J. Liao and E. Shuryak, Phys. Rev. D **82**, 094007 (2010).
[18] P. Danielewicz, Annals Phys. **152**, 239 (1984).
[19] B. Svetitsky, Phys. Rev. D **37**, 2484 (1988).
[20] H. van Hees, M. Mannarelli, V. Greco, and R. Rapp, Phys. Rev. Lett. **100**, 192301 (2008).
[21] H. van Hees and R. Rapp, Phys. Rev. C **71**, 034907 (2005).
[22] A. Adare *et al.* (PHENIX), Phys. Rev. Lett. **98**, 172301 (2007).
[23] R. Rapp, P. B. Gossiaux, A. Andronic, R. Averbeck, S. Masciocchi, *et al.*, (2018), arXiv:1803.03824 [nucl-th].
[24] S. Caron-Huot and G. D. Moore, Phys. Rev. Lett. **100**, 052301 (2008).
[25] M. He, R. J. Fries, and R. Rapp, Phys. Rev. C **86**, 014903 (2012).
[26] R. Rapp and H. van Hees, (2008), arXiv:0803.0901 [hep-ph].
[27] L. Ravagli and R. Rapp, Phys. Lett. B **655**, 126 (2007).
[28] B. Abelev *et al.* (ALICE Collaboration), JHEP **1209**, 112 (2012).
[29] B. Abelev *et al.* (ALICE), Phys. Rev. Lett. **111**, 102301 (2013).
[30] A. M. Sirunyan *et al.* (CMS), (2017), arXiv:1708.04962 [nucl-ex].
[31] M. Nahrgang, J. Aichelin, S. Bass, P. B. Gossiaux, and K. Werner, Phys. Rev. C **91**, 014904 (2015).
[32] J. Noronha-Hostler, B. Betz, J. Noronha, and M. Gyulassy, Phys. Rev. Lett. **116**, 252301 (2016).
[33] C. A. G. Prado, J. Noronha-Hostler, R. Katz, A. A. P. Suaide, J. Noronha, M. G. Munhoz, and M. R. Cosentino, Phys. Rev. C **96**, 064903 (2017).
[34] S. Cao, L.-G. Pang, T. Luo, Y. He, G.-Y. Qin, and X.-N. Wang, Nucl. Part. Phys. Proc. **289-290**, 217 (2017).